magnetochemistry

MDPI

*Article*

# Optimized Design of Permanent Magnet Trip Device Based on Orthogonal Experiments and BP-NSGA-II

**Jie Zhang [1], Yimin You [2,3], Kaicai Zhuo [2,3,*], Lu Zhu [1], Dongyun Dai [2,3], Jun Xiao [1], Junxiang Liu [1] and Yong Wang [1]**

[1] Electric Power Research Institute, Guangzhou Power Supply Bureau, Guangdong Power Grid Corporation Limited, Guangzhou 510510, China; zjllshow@163.com (J.Z.); zhulu@guangzhou.csg.cn (L.Z.); xiaojun@guangzhou.csg.cn (J.X.); liujunxiang@guangzhou.csg.cn (J.L.); wangyong@guangzhou.csg.cn (Y.W.)
[2] School of Electrical Engineering and Automation, Xiamen University of Technology, Xiamen 361024, China; youyimin@126.com (Y.Y.); dongy82@163.com (D.D.)
[3] Xiamen Key Laboratory of Frontier Electric Power Equipment and Intelligent Control, Xiamen 361024, China
* Correspondence: 2322141034@s.xmut.edu.cn; Tel.: +86-17750652570

**Abstract**

To address the issues of slow operation and high variability in traditional electromagnetic trip devices, this paper proposes a magnetic trip device based on the principle of “permanent magnet holding, spring driving, and electric reset,” thereby reducing the circuit breaker tripping time. However, its high material and manufacturing costs have limited its widespread adoption. To address this issue, this paper employs a method combining orthogonal experiments with BP-NSGA-II. Using permanent magnet dimensions, coil wire gauge, moving component mass, and spring initial force as variables, the number of simulations is reduced through orthogonal experiments, and transient electromagnetic simulation is utilized to analyze the trip mechanism’s dynamic performance; a BP neural network surrogate model was constructed to replace finite element simulation, and the NSGA-II algorithm was employed to perform weightless Pareto optimization, with the volume of the permanent magnet and the amount of copper used in the coil as the cost optimization objectives. Under the constraint of a trip time $\leq$ 15 ms, the permanent magnet dimensions were reduced from 8 $\times$ 44 $\times$ 5 mm to 6.5 $\times$ 44 $\times$ 5 mm (a 18.7% reduction in volume), and the coil wire diameter was optimized from 0.18 mm (2000 turns) to 0.14 mm (1400 turns) (a 22.3% reduction in copper usage). Test results show that the optimized trip time was reduced from 16.0 ms to 14.1 ms, with the prototype measuring 14.56 ms in actual testing; the discrepancy between the simulation and experiment was less than 5%. This method provides a reference for the design of a permanent magnet trip device and holds significant engineering value.

**Keywords:** permanent magnet trip device; Maxwell simulation; multi-objective optimization; operating characteristics

Check for updates

Academic Editor: Carlos J. Gómez García

Received: 20 April 2026
Revised: 18 May 2026
Accepted: 26 May 2026
Published: 1 June 2026



## 1. Introduction

A circuit breaker is a critical protective device in power systems whose core function is to rapidly and reliably interrupt fault or overload currents during short circuits or overloads in circuits, thereby safeguarding the safe operation of electrical equipment and power systems [1]. Most circuit breakers on the market employ spring mechanisms to perform the tripping function. The tripping time of the spring mechanism consists of the operating time of the mechanism and the tripping time of the trip device. The operating time of the mechanism is related to its own mechanical components within the transmission system, accounting for a relatively small and fixed proportion. In contrast, the operating time of the trip device is influenced by external factors such as control voltage, exhibiting significant variability and constituting over 50% of the circuit breaker's overall tripping time [2]; therefore, reducing the trip device's response time is an effective means of shortening the circuit breaker's opening time.

The existing spring-operated trip mechanism employs a solenoid-type electromagnetic trip device, whose moving armature undergoes two distinct phases during operation: engagement and movement [3]. Due to the need to overcome the spring reaction force and friction while driving the iron core to accelerate during the actuation phase, the actuation time is relatively long and the iron core's movement velocity often exceeds 2 $m \cdot s^{-1}$. This results in excessive impact force and is susceptible to control voltage fluctuations, causing the circuit breaker's tripping time to vary between 25 and 40 milliseconds, making it difficult to meet the design requirement for tripping within 20 milliseconds [4]. Therefore, Reference [5] employs a permanent magnet trip device to achieve the design requirement of tripping a 12 kV pole-mounted vacuum circuit breaker within 15–20 ms. Compared to solenoid-type electromagnetic trip devices, permanent magnet trip devices employ a coordinated magnetic circuit design combining permanent magnets and coils. A pre-compressed spring drives the moving iron core, offering significant advantages in speed, operational stability, and power consumption [6,7]. However, its structural design presents dual challenges: one is that its dynamic characteristics exhibit electromagnetic and mechanical coupling properties, resulting in low material utilization efficiency; second, high-performance permanent magnet materials are relatively expensive, resulting in higher material and manufacturing costs compared to electromagnetic trip devices. Therefore, it is necessary to reduce the operating time of permanent magnet trip devices while simultaneously lowering their material and manufacturing costs.

The optimization design of the permanent magnet trip device involves single-objective factor analysis [6] and multi-objective factor analysis [8–11]. However, single-objective factor analysis struggles to effectively analyze the synergistic effects of multiple parameters, preventing the achievement of optimal dynamic performance; consequently, multi-objective factor analysis is now commonly employed. For example, Reference [12] applied grey correlation and response surface methods to optimize the dynamic performance of AC contactors, constructing predictive models for spring parameters, contact bounce, and switching speeds, which effectively reduced contact bounce after optimization. Reference [13] employed a multi-step optimization method for the cooperative design of a monostable permanent magnet actuator, effectively meeting its rapid breaking requirements. Compared to the aforementioned comprehensive objective factor optimization methods, the orthogonal experimental design method offers advantages such as a reduced number of experiments and intuitive analysis of factor influences [14–16]. However, using orthogonal experiments alone makes it difficult to fully capture the complex nonlinear relationship between input parameters and dynamic responses. Furthermore, in multi-objective optimization, the introduction of subjective biases through arbitrary weighting often prevents the achievement of unweighted global optimization. In recent years, intelligent optimization algorithms aided by surrogate models have gradually emerged as an effective means of addressing complex electromagnetic mechanism optimization problems. For example, Reference [17] employed a backpropagation (BP) neural network to replace finite element simulation, combining it with a genetic algorithm to optimize an electromagnetic repulsion mechanism; Reference [18] conducted multi-objective optimization design of the permanent magnet operating mechanism for high-voltage vacuum circuit breakers based on an adaptive Kriging surrogate model and the NSGA II algorithm; Reference [19] compared the accuracy of BP neural networks, support vector regression, and Kriging models, verified the high accuracy of the Kriging model, and combined the improved Jaya algorithm with the Kriging model for the multi-objective optimization of electromagnetic devices. However, existing research still rarely considers the multi-objective trade-offs among electromagnetic, mechanical, and cost factors simultaneously and often overlooks the impact of deep interactions between parameters on optimization efficiency.

The strong electromagnetic–mechanical–permanent magnet coupling characteristics of permanent magnet trip devices lead to deep parameter interactions, making traditional methods prone to getting stuck in local optima. To address this, this paper proposes a collaborative optimization framework that combines orthogonal experiments with BP-NSGA-II to achieve unweighted multi-objective Pareto optimization. This approach ensures shorter trip response times while improving the utilization rate of permanent magnet materials and reducing manufacturing costs, thereby providing a new technical pathway for the development of a permanent magnet trip device.

## 2. Structure and Working Principle of Permanent Magnet Trip Devices

### *2.1. Structure and Component Materials of Permanent Magnet Trip Devices*

The structure of the permanent magnet trip device is shown in Figure 1. It primarily consists of a moving core, stationary core, permanent magnet, reaction spring, coil, and coil frame. The permanent magnet trip device adopts a combined electromagnetic-permanent magnet design and features a dual-coil DC excitation system. The key magnetic circuit components—the magnetic yoke, moving iron core, and stationary iron core—are all fabricated from DT4C electrical pure iron material. This material exhibits high magnetic permeability and low coercivity, facilitating rapid establishment and decay of the magnetic field. The drive guide rod, limit housing, reaction spring, and other mechanical structural components are constructed from non-magnetic stainless steel materials to prevent stray magnetic field interference, thereby ensuring precise control of the moving iron core's travel distance. Permanent magnets utilize sintered neodymium iron boron N35H material, whose high coercivity and high energy product provide a stable holding force [20], ensuring that the permanent magnet trip device reliably engages during power failure.

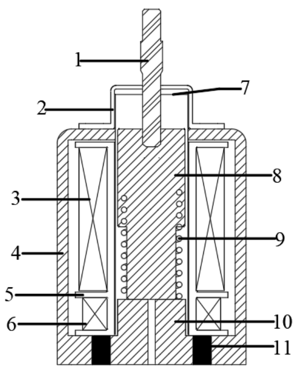


**Figure 1.** Structure of permanent magnet trip device. 1—Drive rod; 2—Limit housing; 3—Reset coil; 4—Magnetic yoke; 5—Coil frame; 6—Tripping coil; 7—Copper sleeve; 8—Moving iron core; 9—Reaction spring; 10—Stationary iron core; 11—Permanent magnet.

### *2.2. Working Principle of Permanent Magnet Trip Device*

Similar to the operating principle of traditional magnetically held switch devices [21], the permanent magnet trip device operates on the principle of "permanent magnet holding–spring actuation–electric reset." During the normal operation of the circuit breaker, no current flows through the trip or reset coil. Instead, the permanent magnet trip device relies solely on the inherent magnetic force of the permanent magnet to maintain the engagement between its moving and stationary cores. A permanent magnet trip device can be subdivided into the tripping process and reset process based on the different directions of movement of the moving iron core: During the tripping process, the reset coil remains de-energized while the trip coil energizes to generate a magnetic field opposing the permanent magnet flux. This reduces the magnetic force between the moving and stationary cores. The moving core is driven by the counterforce spring, causing it to actuate. The direction of the magnetic flux and trip coil current is shown in Figure 2a. During the reset process, the trip coil is de-energized while the reset coil is energized, generating a magnetic field that reinforces the direction of the permanent magnet flux. The electromagnetic force produced by the energized reset coil, combined with the inherent magnetic force of the permanent magnet, drives the moving iron core back to the engaged position. Simultaneously, the counterforce spring is compressed, storing energy for the next trip operation. The directions of the magnetic flux and reset coil current are shown in Figure 2b.

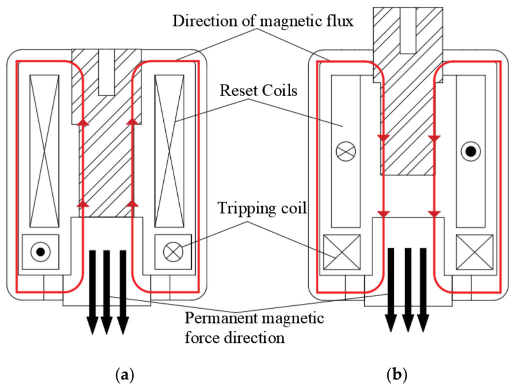


**Figure 2.** Magnetic flux and current direction during tripping and reset process of permanent magnet trip device. (**a**) Tripping Process; (**b**) Reset Process.

*2.3. Design Specifications for Permanent Magnet Trip Device*

- The permanent magnet trip device shall have a tripping time not exceeding 15 ms at a rated voltage of DC 220 V, with the peak current of the trip coil not exceeding 1.5 A.
- It shall meet the performance requirements for a trip device specified in GB/T 11022-2020 "Common Technical Requirements for High-Voltage AC Switchgear and Control Gear" [22]: The trip coil must reliably trip at 65% rated voltage and above, and must not trip at 30% rated voltage and below.
- Without requiring external mechanical structures, the permanent magnet trip device shall achieve automatic and reliable reset functionality through the operation of the reset coil.

## 3. Simulation Analysis of Permanent Magnet Trip Device

*3.1. Simulation Modeling*

This study employs Maxwell finite element ansys 19.2 software to perform simulation analysis on a permanent magnet trip device. Since the structure of a permanent magnet release is not axisymmetric, and the performance of the permanent magnet depends largely on the direction of magnetization, Maxwell 2D—which is only suitable for infinitely long or axisymmetric structures—is limited to in-plane or radial/axial magnetization directions. Consequently, it cannot accurately describe the three-dimensional magnetic field distribution of the permanent magnet, making it difficult to reflect the actual direction of the attractive force acting on the permanent magnet trip. In contrast, Maxwell 3D supports the configuration of magnetization vectors in any direction, enabling a more accurate representation of the magnetic circuit and magnetic field distribution within the permanent magnet trip device. Therefore, this paper employs Maxwell 3D to simulate the dynamic characteristics of the permanent magnet trip device, with the specific workflow illustrated in Figure 3.

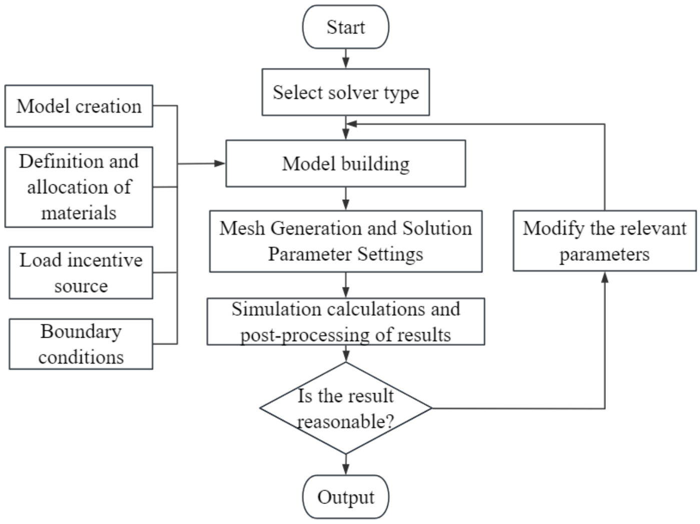


**Figure 3.** Maxwell Simulation Flowchart.

Following the specific steps of the simulation process described above, complete the simulation modeling of the permanent magnet trip device, configure the materials and motion parameters for each component, and add excitation sources.

(1) Model Simplification and Mesh Generation.

To enhance computational efficiency and accuracy, non-ferromagnetic materials that do not affect magnetic circuit calculations are removed using 3D modeling software. In the design of motion domains and moving components, curved surfaces should be avoided. Instead, a regular dodecagonal prism should be used to approximate the cross-section of the cylindrical iron core, with the surface area error controllable within 0.05 $mm^2$. When performing mesh partitioning, the internal mesh partitioning method is selected, with a focus on refining the mesh in the motion domain and moving components. The remaining components can be appropriately simplified to enhance computational efficiency. The simulation model and mesh partitioning results are shown in Figure 4.

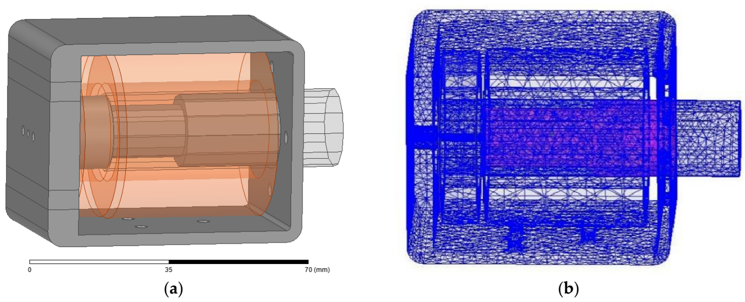


**Figure 4.** Permanent magnet trip device simulation model and mesh division. (**a**) Simulation Model; (**b**) Mesh Partitioning.

(2) Material Simulation Settings.

For material settings, the simulation model materials were added based on the permanent magnet trip device materials described in Section 2.1. Because the DT4C material is not included in the software's built-in library, the relevant material properties must be defined using the software's Material Library Manager. We obtain the B-H values for DT4C according to Electromagnetic Pure Iron: GB/T 6983-2022 [23]. After inputting the B-H values, the software automatically fits the curve and generates the B-H curve shown in Figure 5.

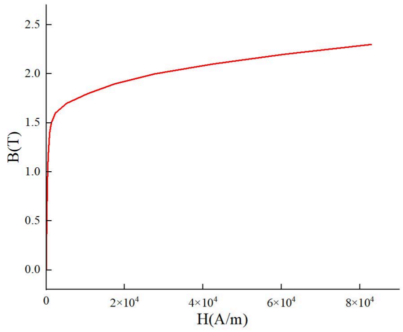


**Figure 5.** B-H curve of DT4C.

(3) Motion Parameter Settings.

The motion domain is set in a linear direction to distinguish tripping/reset. The motion component is configured with a mass of 128.9 g, damping of 2.453 (N·s/m), spring load parameters (55–30 N), and breaker trip latch release force load parameters (20–25 N). Additionally, we note that the moving iron core has a stroke of 11 mm. The moving iron core's motion range must not exceed the 20 mm area restricted by the motion domain.

(4) Incentive Source Configuration.

The transient electromagnetic field simulation employs an external circuit approach to apply coil excitation, utilizing the software's Circuit Editor to construct the coil circuit. The permanent magnet trip device coil can be equivalent to a series connection of resistance and inductance. The freewheeling diode is connected in parallel with the permanent magnet trip coil to reduce overvoltage during the instantaneous opening of the coil circuit. The voltage-controlled switch (SSVK) employs a level drive, controlling the conduction of the coil circuit by adjusting the duty cycle of the drive voltage. The control circuit for the permanent magnet trip device coil is shown in Figure 6. We set the coil excitation voltage source to DC 220 V, with the trip coil resistance value at 145 Ω and the trip coil turns at 2000 turns. The reset coil has a resistance value of 80 Ω and a winding count of 3000 turns.

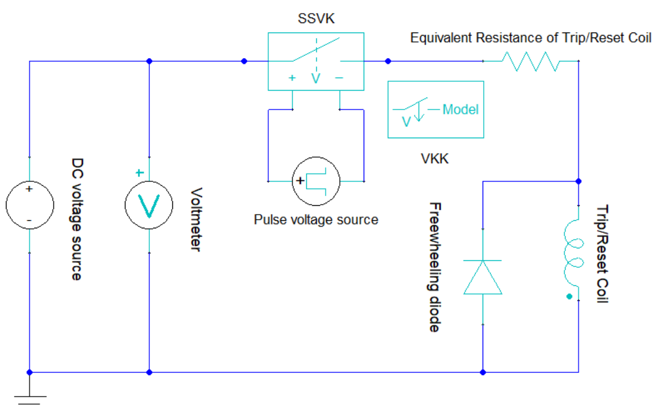


**Figure 6.** Control circuit for permanent magnet trip device coil.

### *3.2. Dynamic Simulation Analysis*

A simulation analysis was conducted on the tripping and resetting processes of a permanent magnet trip device operating at a rated voltage of DC 220 V, yielding the operational characteristic curves for these processes, as shown in Figures 7 and 8.

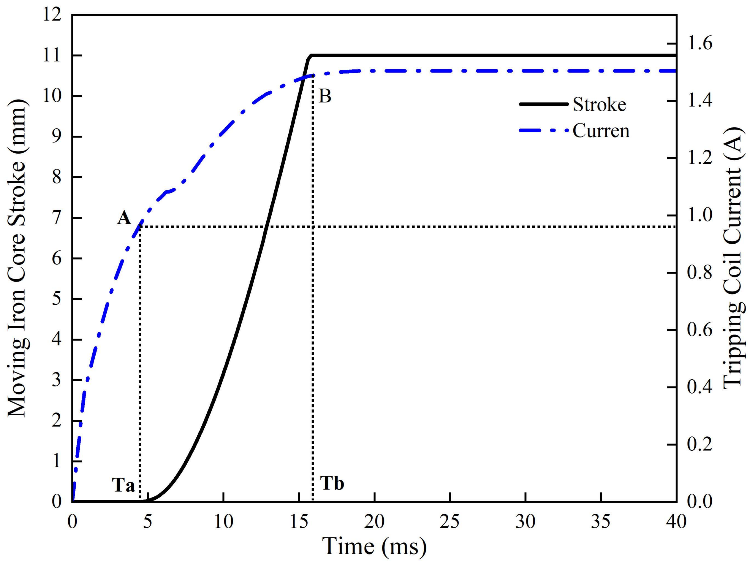


**Figure 7.** Stroke of moving iron core and current curve of trip coil.

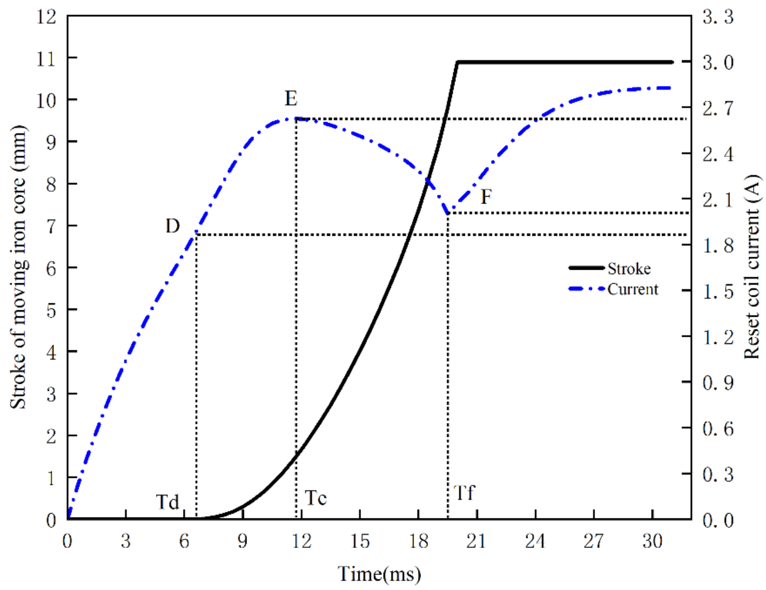


**Figure 8.** Stroke of moving iron core and reset coil current curve.

The tripping process is divided into two stages based on the differences in the movement of the moving iron core: the initiation stage (0–T*a*) and the motion stage (T*a*–T*b*). During the actuation phase (0–T*a*), the moving iron core remains stationary as the magnetic force exceeds the spring's initial force (55 N), causing the trip coil current to rise rapidly. Upon entering the movement phase (T*a*–T*b*), when the current increases to point A (0.746 A), the permanent magnet's magnetic force becomes insufficient to maintain engagement, causing the moving iron core to begin moving. Movement induces changes in magnetic flux, generating a countercurrent in the coil that suppresses current growth. As the air gap widens, the moving iron core accelerates, the rate of change in magnetic flux increases, and the current rise slows. At T*b* (16.0 ms), the permanent magnet trip device completes its tripping action.

The reset process can also be divided into three stages based on the differences in the armature's movement: the initial contact stage (0–T*d*), movement stage (T*d*–$T_f$), and stable holding stage (after $T_f$). During the 0–T*d* phase, the magnetic force acting on the moving iron core is less than the spring's release force (30 N), maintaining the non-release state. The reset coil stores energy, and the current rises rapidly. During the T$d$–T$_f$ phase, the magnetic force exceeds the spring's final release force (30 N), causing the moving iron core to begin moving. Initially, the movement is slow, with minimal changes in magnetic flux. The reverse current increases gradually, while the coil current continues to rise. At the moment of transition, the rate of increase in the reverse counter-electromotive force current equals the rate of increase in the coil current. Subsequently, under the combined action of electromagnetic and permanent magnet forces, the moving iron core accelerates. The counter-electromotive force generated by its motion inhibits current growth, causing the current to begin decreasing. When the armature is fully engaged, the movement ceases. Thereafter, the counter-electromotive force of the movement disappears. To maintain voltage equilibrium, the coil current rises again until it stabilizes.

Based on the simulation results, the main technical parameters of the permanent magnet trip device have been determined, as shown in Table 1.

**Table 1.** Key technical parameters of permanent magnet trip device.

| Parameter Type | Numerical Value |
|---|---|
| Coil rated voltage/V | DC220 |
| Magnetic yoke thickness /mm | 3 |
| Permanent magnet/mm | 44 × 8 × 5 (L × H × W) |
| Tripping coil Wire diameter/mm | 0.18 |
| Trip coil resistance/Ω | 140 ± 2 |
| Tripping coil turns/N | 2000 ± 50 |
| Reset coil wire diameter/mm | 0.29 |
| Reset coil resistance/Ω | 80 ± 2 |
| Reset coil turns/N | 3000 ± 50 |
| Moving iron Moving component mass/g | 128.9 |
| Bolt release force/N | 20–25 |
| Reaction spring force/N | 55–30 |

## 4. Parameter Optimization Based on Orthogonal Experiments and BP-NSGA-II

Since the simulation-based tripping time of the initial design was 16.0 ms, which did not meet the design requirements, its tripping performance needs to be optimized. Based on the electromagnetic-mechanical coupling dynamics of the permanent magnet trip device and the equations governing its motion, it is known that the size of the permanent magnet affects the holding force: a larger magnet provides stronger resistance to false tripping but requires a higher number of reverse ampere-turns, which prolongs the actuation time and increases power consumption; the wire gauge of the coil determines the ampere-turns and resistance, and there is an optimal match between them; the mass of the moving parts affects inertia and must be matched with the spring force to control impact; The spring force serves as the driving force; increasing it can shorten the actuation time but makes reset more difficult. Since these parameters are mutually coupled, optimization is not a matter of adjusting parameters in isolation, but rather of seeking the optimal balance between the permanent magnet holding force, the electromagnetic counterforce, the spring driving force, and the inertial force. This paper focuses on optimizing these four parameters to shorten the tripping time, improve material utilization, and reduce costs.

$$\frac{F_1 - F - f}{m} = \frac{d^2 s}{dt^2} \tag{1}$$

In the equation: $F_1$ represents the spring driving force during the tripping process (N); $F$ represents the magnetic force acting on the core during the corresponding process

(N); $f$ represents the sum of all resistive forces acting on the core during its motion (N); $m$ represents the mass of the moving component (g); and $s$ represents the stroke of the moving core (m).

### *4.1. Design of an Orthogonal Array and Analysis of Results*

#### 4.1.1. Orthogonal Array Design

The dimensions of the permanent magnet, the wire gauge of the trip coil, the spring driving force, and the mass parameters of the moving components prior to the optimization of the permanent magnet trip device are shown in Table 2. These four parameters are denoted as A, B, C, and D, respectively. Three levels were selected for each factor, with the selection of each level determined based on engineering and manufacturing constraints, pre-simulation boundaries, and technical standard requirements, as shown in Table 3.

**Table 2.** Parameters of permanent magnet trip device.

| Parameter Type | Permanent Magnet/mm | Tripping Coil Wire Diameter/mm | Moving Component Mass/g | Initial Force of Reaction Spring/N |
|---|---|---|---|---|
| Pre-optimization parameters | 5 × 8 × 44 | 0.18 | 128.9 | 55 |

**Table 3.** Permanent magnet trip device test parameter combinations.

| Level \ Factor | A | B | C | D |
|---|---|---|---|---|
| | Permanent Magnet/mm | Tripping Coil Wire Diameter/mm | Moving Component Mass/g | Initial Force of Reaction Spring/N |
| Level 1 | 5 × 8 × 44 | 0.14 | 128.9 | 65 |
| Level 2 | 5 × 6.5 × 44 | 0.16 | 114.1 | 60 |
| Level 3 | 5 × 8 × 30 | 0.18 | 102.4 | 55 |

As shown in Table 3, this optimization experiment employs a four-factor, three-level design. Given that there is no inherent relationship between the factors, an L9($3^4$) orthogonal array was selected for the experiment to balance simulation efficiency with the representativeness of the results. The use of this array enables the acquisition of key information from a comprehensive experiment with only nine simulations, thereby significantly improving optimization efficiency whilst ensuring the reliability of the results and demonstrating good engineering applicability and feasibility [24]. The specific experimental combinations and simulation results are detailed in Table 4.

**Table 4.** The specific test combinations.

| Level \ Factor | A | B | C | D |
|---|---|---|---|---|
| | Permanent Magnet/mm | Tripping Coil Wire Diameter/mm | Moving Component Mass/g | Initial Force of Reaction Spring/N |
| Level 1 | 5 × 8 × 44 | 0.14 | 128.9 | 65 |
| Level 2 | 5 × 8 × 44 | 0.16 | 114.1 | 60 |
| Level 3 | 5 × 8 × 44 | 0.18 | 102.4 | 55 |
| Level 4 | 5 × 6.5 × 44 | 0.14 | 114.1 | 55 |
| Level 5 | 5 × 6.5 × 44 | 0.16 | 102.4 | 65 |
| Level 6 | 5 × 6.5 × 44 | 0.18 | 128.9 | 60 |
| Level 7 | 5 × 8 × 30 | 0.14 | 102.4 | 60 |
| Level 8 | 5 × 8 × 30 | 0.16 | 128.9 | 55 |
| Level 9 | 5 × 8 × 30 | 0.18 | 114.1 | 65 |

4.1.2. Results and Analysis of the Orthogonal Experiment

Based on the level parameters of the four factors determined in Table 4, the simulation model was modified and the parameters reset, and dynamic characteristic simulations were carried out. The simulation results for the engagement time, operating time, disengagement speed and coil current were recorded; the simulation results are shown in Table 5.

**Table 5.** Simulation results for different parameter combinations.

| Factor / Level | Simulation Results | | | |
|---|---|---|---|---|
| | Touch Time/ms | Tripping Time/ms | Tripping Speed/m·s$^{-1}$ | Peak Current/A |
| Level 1 | 3.8 | 15.7 | 1.43 | 1.428 |
| Level 2 | 4.0 | 15.1 | 1.45 | 1.440 |
| Level 3 | 6.2 | 17.8 | 1.41 | 1.340 |
| Level 4 | 3.6 | 15.6 | 1.32 | 1.436 |
| Level 5 | 2.4 | 12.2 | 1.66 | 1.457 |
| Level 6 | 3.5 | 14.6 | 1.34 | 1.402 |
| Level 7 | 2.6 | 12.6 | 1.53 | 1.495 |
| Level 8 | 2.3 | 13.8 | 1.23 | 1.470 |
| Level 9 | 2.3 | 12.2 | 1.55 | 1.385 |

The methods used to analysis orthogonal experiments include analysis of variance (ANOVA) and range analysis. As range analysis offers advantages such as lower computational demands and more intuitive results [25], this method is employed to analysis the simulation results. The specific formulae are as follows:

Level mean: The arithmetic mean of the corresponding measure across all experimental groups when a particular experimental factor $X$ is at level $i$. It is expressed as

$$\overline{y}_{Xi} = \frac{1}{k}\sum_{j=1}^{k} y_{Xij} \tag{2}$$

where $\overline{y}_{Xi}$ is the mean of the experimental indicator at the $i$-th level of factor $X$; $k$ is the number of trials when factor $X$ is at the $i$-th level; and $y_{Xij}$ is the specific value of the experimental indicator for the $j$-th group when factor $X$ is at the $i$-th level.

Range: the difference between the maximum and minimum mean values of the measured variable y at each level of the experimental factor $X$. It is expressed as

$$R_X = \max(\overline{y}_{X1}, \overline{y}_{X2}, \ldots, \overline{y}_{Xn}) - \min(\overline{y}_{X1}, \overline{y}_{X2}, \ldots, \overline{y}_{Xn}) \tag{3}$$

where $R_X$ is the range of the experimental measure for factor $X$; $n$ is the number of levels of factor $X$; $\overline{y}_{X1}, \overline{y}_{X2}, \ldots, \overline{y}_{Xn}$ is the mean of the measure for each level of factor $X$.

Rank the ranges of the experimental factors for the same experimental parameter from largest to smallest; the larger the range, the more significant the influence of that factor on the experimental parameter, that is

$$R_{X1} > R_{X2} > \cdots > R_{Xm} \Rightarrow X1 > X2 > \cdots > Xm \tag{4}$$

where $m$ is the total number of factors selected for the experiment.

Using the formulae for calculating the mean and range, the nine sets of data in Table 5 were analysed to obtain the means and ranges for each factor, as shown in Table 6.

**Table 6.** Mean and range of parameter simulation results.

| Factor / Level | Touch Time/ms | | Tripping Time/ms | | Tripping Speed/m·s$^{-1}$ | | Peak Current/A | |
|---|---|---|---|---|---|---|---|---|
| | Mean | Range | Mean | Range | Mean | Range | Mean | Range |
| A1 | 4.67 | | 16.2 | | 1.73 | | 1.403 | |
| A2 | 3.17 | 2.27 | 14.13 | 3.33 | 1.74 | 0.01 | 1.432 | 0.047 |
| A3 | 2.4 | | 12.87 | | 1.74 | | 1.45 | |
| B1 | 3.33 | | 14.63 | | 1.73 | | 1.453 | |
| B2 | 2.9 | 1.1 | 13.7 | 1.17 | 1.75 | 0.02 | 1.456 | 0.08 |
| B3 | 4 | | 14.87 | | 1.73 | | 1.376 | |
| C1 | 3.2 | | 14.7 | | 1.63 | | 1.433 | |
| C2 | 3.3 | 0.53 | 14.3 | 0.50 | 1.74 | 0.20 | 1.42 | 0.013 |
| C3 | 3.73 | | 14.2 | | 1.83 | | 1.431 | |
| D1 | 2.83 | | 13.37 | | 1.85 | | 1.423 | |
| D2 | 3.37 | 1.2 | 14.1 | 2.36 | 1.74 | 0.23 | 1.446 | 0.031 |
| D3 | 4.03 | | 15.73 | | 1.62 | | 1.415 | |

From Equation (4), it can be seen that the factors influencing the trigger time of the permanent magnet trip device are ranked as follows: A > D > B > C; the factors influencing the trip action time are ranked as follows: A > D > B > C; the factors influencing the trip speed are ranked as follows: D > C > B > A; and the factors influencing the coil current are ranked as follows: B > A > D > C.

When different levels of a factor have varying effects on an indicator, this indicates the presence of a main effect. Based on the mean values in Table 6, main effect plots for the means of each indicator were constructed, as shown in Figure 9. In the main effect plot, if the line connecting the points is horizontal, this indicates that the factor has no significant effect on the indicator; conversely, the greater the difference in the span of the line, the more significant the effect of the factor on the indicator.

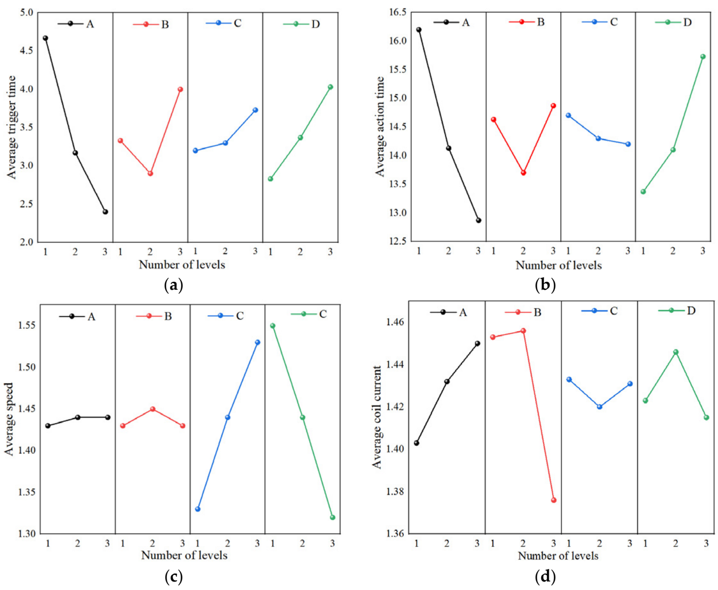


**Figure 9.** Main effect plot of the mean. (**a**) trigger time; (**b**) action time; (**c**) trip speed; (**d**) coil current.

For a permanent magnet trip device, it is desirable for the engagement time and trip time to be as short as possible, for the trip coil current to be as low as possible, and for the trip speed to be as low as possible. Based on the main effect plots for each parameter shown in Figure 9, the optimal combination of parameters for trigger time is $A_3B_2C_1D_1$; for tripping time, it is $A_3B_2C_3D_1$; for tripping speed, it is either $A_1B_1C_1D_3$ or $A_1B_3C_1D_3$; and for coil current, it is $A_1B_3C_2D_3$. It is evident that the optimal combinations for each parameter are not consistent; the above individual analyses cannot achieve an optimal state for all objectives simultaneously.

### *4.2. Multi-Objective Optimization of Permanent Magnet Trip Device Based on BP-NSGA-II*

As orthogonal experiments can only determine the order of importance of each factor's influence and the optimal combination for a single objective, they cannot directly establish a continuous non-linear mapping relationship between the optimization variables and performance indicators. Consequently, it is difficult to achieve global optimization, and multi-objective coordinated optimization cannot be accommodated. To address this, a simulation proxy model of a permanent magnet trip device is constructed using a back-propagation (BP) neural network based on orthogonal experiments, and multi-objective optimization design is carried out using the NSGA-II algorithm.

#### 4.2.1. Model for Multi-Objective Optimization of Permanent Magnet Trip Device

The multi-objective optimization problem for the permanent magnet trip device can be described as follows: subject to the condition that the trip action time is ≤15 ms, the objective is to achieve a fast trip action time and actuation time, low trip speed, low coil current and low cost, thereby achieving an overall optimum balance of fast response, low impact, low power consumption and low cost. The mathematical model is shown in Equation (4).

$$\begin{cases} X = [A, B, C, D]^T \\ \min F(X) = [T_1(X), T_2(X), v(X), I(X), C_o(X)]^T \\ \text{s.t. } T_2(X) \leq 15 \text{ ms} \end{cases} \tag{5}$$

In the formula, $X$ represents the combination of inputs for each factor.

The cost of a permanent magnet trip device is composed of its various components, with the materials for the permanent magnets and the copper wire for the coils accounting for a significant portion of the total cost, while the remaining components account for a smaller portion. Let $W_1$, $W_2$, and $W_3$ represent the weighting coefficients for the costs of the permanent magnet, the copper wire for the coil, and other components, respectively, such that $W_1 + W_2 + W_3 = 1$. Using the pre-optimization design as the baseline (with a cost coefficient of 1), the formula for calculating the cost coefficient of the permanent magnet trip device is

$$C = W_1 \cdot \frac{V_{\text{mag}}}{V_{\text{mag0}}} + W_2 \cdot \frac{M_{\text{cut}}}{M_{\text{cut0}}} + W_3 \cdot \frac{P_{\text{other}}}{P_{\text{other0}}} \tag{6}$$

In the formula: $X$ represents the combination of inputs for each factor. In the equation: $V_{\text{mag}}$ is the volume of the permanent magnet, and $V_{\text{mag0}}$ is the volume of the permanent magnet before optimization; $M_{\text{cu}}$ is the mass of copper used in the trip coil, and $M_{\text{cu0}}$ is the mass of copper used before optimization; $P_{\text{other}}$ is the cost of other components, and $P_{\text{other0}}$ is the cost of other components before optimization. Based on actual cost proportions in engineering practice, this paper sets $W_1$= 0.4, $W_2$ = 0.35, and $W_3$ = 0.25.

#### 4.2.2. Construction of a Proxy Model Based on a Backpropagation Neural Network

The BP neural network is a multi-layer feedforward network with strong nonlinear mapping capabilities [26]. In this paper, it is used to construct a proxy model for a permanent magnet trip mechanism. The model inputs consist of four optimization variables: permanent magnet dimensions, coil wire gauge, mass of moving components, and spring driving force. The outputs comprise five performance metrics: actuation time, operating time, trip speed, peak coil current, and cost coefficient. Since orthogonal experiments with only nine sample sets are prone to overfitting, Latin hypercubic sampling was employed to generate an additional 16 combinations within the same parameter space, resulting in a total of 25 sample sets. Performance data for each set was obtained through Maxwell 3D transient simulation. The data was randomly divided into training and testing sets in an 8:2 ratio. The network employs a two-hidden-layer structure (with 8 and 4 hidden device, respectively) and uses the ReLU activation function to establish a nonlinear mapping from input to output [27]. The specific implementation is as follows:

(1) From the input layer to the first hidden layer:

$$H_1 = f(W_1 \cdot X + b_1) \tag{7}$$

where $W_1$ is the input layer weight matrix; $b_1$ is the bias of the first hidden layer; $f$ is the *ReLU* activation function; and, $X = [x_1, x_2, x_3, x_4]^T$, $x_1, x_2, x_3, x_4$ represent the dimensions of the permanent magnet, the wire gauge of the coil, the mass of the moving component, and the driving force of the spring, respectively.

(2) From the first hidden layer to the second hidden layer:

$$H_2 = f(W_2 \cdot H_1 + b_2) \tag{8}$$

where $W_2$ is the weight matrix of the first hidden layer, and $b_2$ is the bias of the second hidden layer.

(3) From the second hidden layer to the output layer:

$$\begin{bmatrix} \hat{T}_1 & \hat{T}_2 & \hat{v} & \hat{I} & \hat{C}_o \end{bmatrix}^T = W_3 \cdot H_2 + b_3 \tag{9}$$

where $\hat{T}_1$ is the predicted trigger time, $\hat{T}_2$ is the predicted trip action time, $\hat{v}$ is the predicted trip speed, $\hat{I}$ is the predicted coil current, and $\hat{C}_o$ is the predicted cost.

Once the surrogate model has been developed, its accuracy must be verified to ensure that it can be used in place of finite element simulation for optimization calculations. This paper adopts the cross-correlation coefficient as the metric for evaluating the accuracy of the surrogate model, as it objectively reflects the degree of agreement between the model's predicted values and the actual values obtained from finite element simulation.

$$R^2 = 1 - \frac{\sum_{i=1}^{m} (y_i - \widetilde{y}_i)^2}{\sum_{i=1}^{m} (y_i - \overline{y})^2} \tag{10}$$

where $y_i$ is the actual value from the finite element simulation, $\widetilde{y}_i$ is the predicted value from the model, $\overline{y}$ is the mean value of the sample data, and $m$ is the total number of test samples.

The fitting accuracy of the BP neural network proxy model established for parameters such as the tripping time and actuation time of the permanent magnet trip device was evaluated; the evaluation results are shown in Table 7.

**Table 7.** Accuracy Evaluation of the BP Neural Network Proxy Model.

| Target Performance | Trip Time | Touch Time | Trip Speed | Coil Current | Cost Factor |
|---|---|---|---|---|---|
| $R^2$ | 0.9796 | 0.9965 | 0.9765 | 0.9775 | 0.9713 |

The cross-correlation coefficient ranges from 0 to 1; the closer the value is to 1, the higher the fitting accuracy of the surrogate model and the smaller the prediction error. When the coefficient exceeds 0.95, the model is considered to have high fitting accuracy and can replace finite element simulation for rapid calculations. As shown in the table, the constructed BP neural network surrogate clearly exhibits high predictive accuracy and effectively maps the nonlinear relationship between the structural parameters and performance parameters of the permanent magnet trip device.

#### 4.2.3. Multi-Objective Optimization Using NSGA-II

NSGA II (Non-dominance Sorting Genetic Algorithm II), as a classic multi-objective optimization algorithm, has been widely applied in fields such as machine learning, resource allocation and engineering design [28]. This algorithm is an improved version of NSGA; it achieves multi-objective optimization solutions through rapid non-dominance sorting and crowding factor calculation, and is capable of effectively evaluating the quality of individuals during the evolutionary process whilst maintaining population diversity. Furthermore, the algorithm incorporates an elite retention mechanism, which ensures that high-performing individuals from the parent population are retained in the offspring population, thereby significantly improving the convergence speed and solution quality of the optimization process. The specific workflow of the NSGA II algorithm is illustrated in Figure 10.

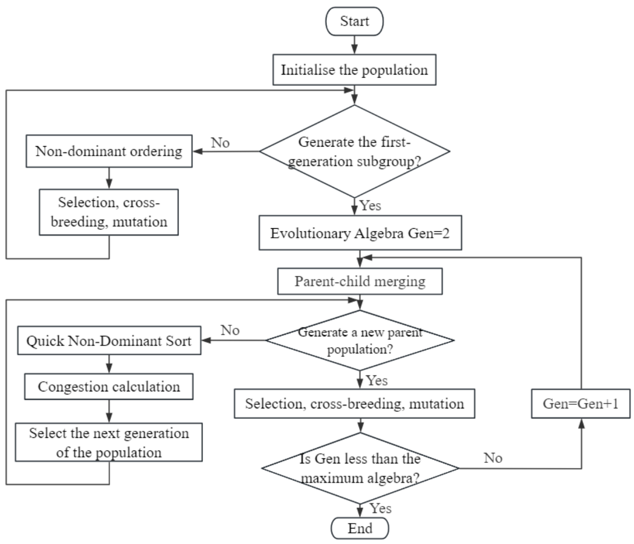


**Figure 10.** Flowchart of the NSGA-II algorithm.

Pareto evaluation is a fundamental criterion for assessing the performance of solution sets in multi-objective optimization problems, and its core is rooted in the Pareto optimality principle. This principle states that in multi-objective optimization, the various objectives are mutually conflicting, and a global optimal solution typically does not exist; instead, a trade-off must be achieved among the different objectives. Pareto evaluation is used to identify a set of optimal solutions, which together form the Pareto front, where each solution is a non-dominated solution.

To balance optimization performance and computational efficiency, the NSGA-II parameters must be set appropriately. The initial population size affects the scope of the global search and the computational load; the number of iterations determines the search depth; the crossover probability balances diversity; and the mutation probability prevents premature convergence. The specific parameter settings for the NSGA-II algorithm are shown in Table 8.

**Table 8.** NSGA-II Algorithm Parameter Settings.

| Parameters | Parameter Value |
|---|---|
| Initial population size | 20 |
| Number of iterations | 100 |
| Cross-probability | 0.9 |
| Probability of mutation | 0.05 |

The NSGA-II algorithm is used to iteratively solve the surrogate model function and the multi-objective optimization model, thereby obtaining a Pareto front diagram following iterative optimization by the NSGA-II algorithm, as shown in Figure 11.

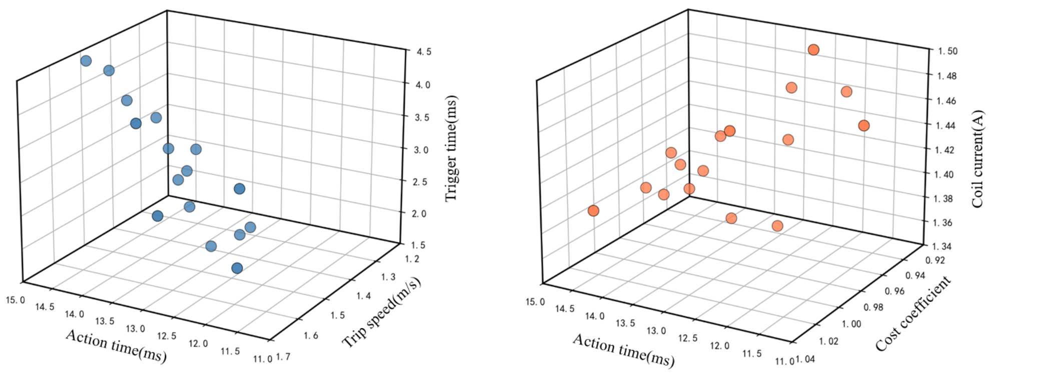


(**a**) (**b**)

**Figure 11.** Pareto chart. (**a**) Action time-trigger speed-actuation time; (**b**) action time-cost coefficient-coil current.

Figure 11 illustrates the distribution of the Pareto front. It can be seen that the trip time essentially meets the requirements. Given that the permanent magnet trip device employs an electrically self-resetting mechanism, there is a trade-off between trip time and reset reliability; simultaneously, the static holding force (which is directly proportional to the size of the permanent magnet) is critical for preventing misoperation. Therefore, the engineering design must balance response speed, reset reliability, and misoperation prevention. Based on the Pareto solution set obtained from the NSGA-II algorithm, a decision-making method based on range sorting of orthogonal experiments was employed. First, solutions satisfying all constraints were screened, then ranked according to the following priorities: constraint satisfaction > operating time > cost factor > peak current. Finally, the optimal combination of parameters was selected, as shown in Table 9.

**Table 9.** Comparison of parameters before and after optimization.

| Factors | A/mm | B/mm | C/g | D/N |
|---|---|---|---|---|
| Value | $5 \times 6.5 \times 44$ | 0.14 | 114.1 | 60 |

The optimal performance parameters obtained using the NSGA-II algorithm are as follows: Action time of 13.86 ms, trigger time of 2.93 ms, cost coefficient of 0.949, coil current of 1.465 A, and tripping speed of 1.45 m/s.

### *4.3. Simulation Analysis of Optimal Combinations*

Given that the algorithm itself is subject to a certain degree of error, the optimised parameters must be validated through Maxwell simulations. The optimal parameter combination $A_2B_1C_2D_2$ obtained from the optimization was applied to the simulation model to perform a further simulation of the permanent magnet trip device, and the results were compared with those prior to optimization. The comparison of performance metrics before and after optimization is shown in Table 10 whilst the comparison of characteristic curves for each metric is illustrated in Figure 12.

**Table 10.** Simulation results.

| Factor / Level | Simulation Results | | | |
|---|---|---|---|---|
| | **Touch Time/ms** | **Tripping Time/ms** | **Tripping Speed/m·s$^{-1}$** | **Peak Current/A** |
| Before Optimization | 4.1 | 15.9 | 1.57 | 1.488 |
| After Optimization | 3.1 | 14.1 | 1.68 | 1.432 |

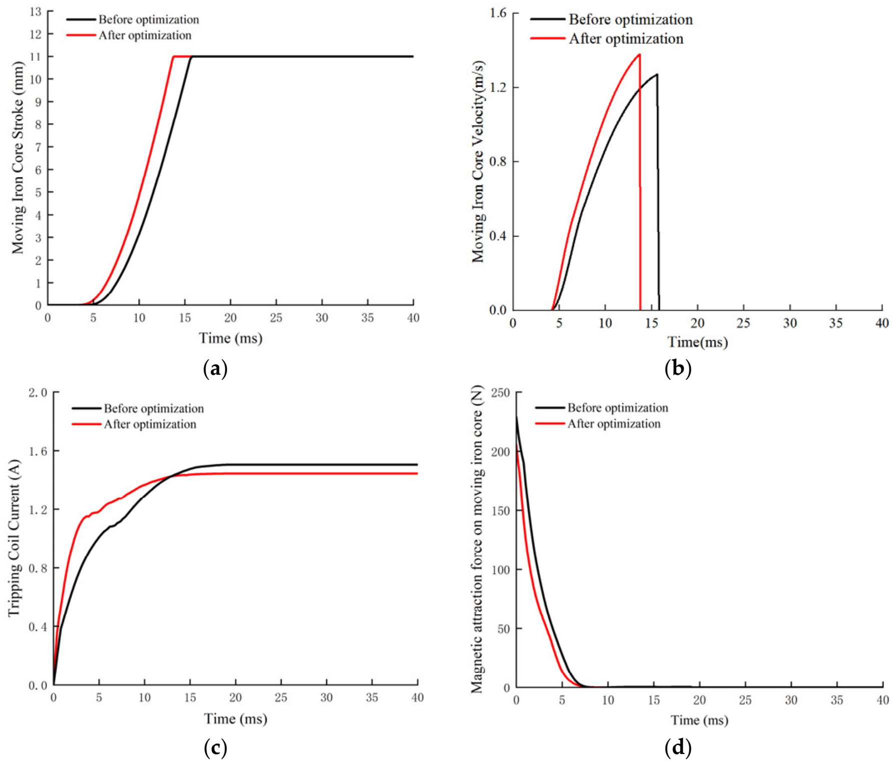


**Figure 12.** Comparison of parameters before and after optimization. (**a**) Displacement curve; (**b**) Speed curve; (**c**) Current curve; (**d**) Suction curve.

As shown in Table 9, the results of the algorithm optimization show only a small deviation from the Maxwell simulation results, meeting the accuracy requirements. Following optimization, the operating time of the permanent magnet trip device was reduced from 16.0 ms to 14.1 ms, a decrease of 11.8%; the coil current was reduced from 1.488 A to 1.432 A, a decrease of 3.8%; the quantities of both the coil and the permanent magnets were reduced compared to before optimization, with the amount of permanent magnet material reduced by 18.75% and the amount of copper wire used in the coil reduced by 25.26%. This has achieved cost optimization, with a slight improvement in tripping speed and a faster dynamic response of the permanent magnet trip device.

To verify whether this optimization scheme meets the requirements of the national standard design, simulations must also be carried out for the trip coil at 65% and 30% of the rated voltage, and for the reset coil at 65% of the rated voltage. The simulation results are shown in Figure 13.

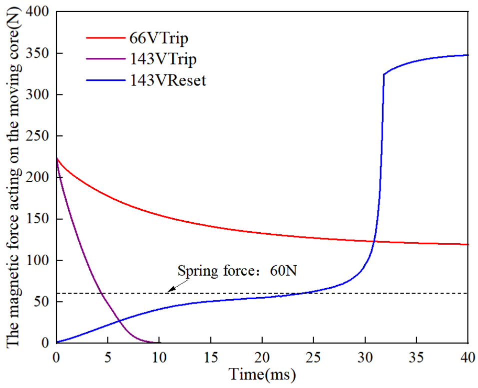


**Figure 13.** Variation in magnetic attraction force on moving iron cores at different voltage levels.

As shown in Figure 13, at 65% of the rated voltage, when the trip coil is energised for longer than 3 ms, the permanent magnetic force acting on the moving core is less than the force (60 N) exerted by the return spring; consequently, the moving and stationary cores cannot maintain the engaged state. As soon as the moving core is disengaged, the magnetic resistance of the circuit increases rapidly, causing the permanent magnetic force acting on the moving core to decrease further. As the permanent magnet trip device employs a counterforce spring drive mechanism, the moving core is ultimately driven by the counterforce spring to achieve reliable tripping. At 30% of the rated voltage, the magnetic attraction acting on the moving core after the trip coil is energised remains greater than the counterforce spring force (60 N); the moving core does not move, and the permanent magnet trip device will not trip. At 65% of the rated voltage, once the reset coil is energised, the magnetic attraction acting on the moving core will exceed the force of the return spring; under the combined action of the reset coil and the permanent magnet, the moving core will complete its reset movement.

## 5. Physical Prototype Performance Testing

Based on the simulation results, the optimized permanent magnet trip device was manufactured and assembled, with its physical prototype shown in Figure 14a. The trip device was installed on a 10 kV/1250 A vacuum circuit breaker from Xiamen XEC Electric Co., Ltd., as depicted in Figure 14b. The test system consists of an adjustable DC power supply, a Hall-effect current sensor, an angular displacement sensor, and a data acquisition device for the test computer.

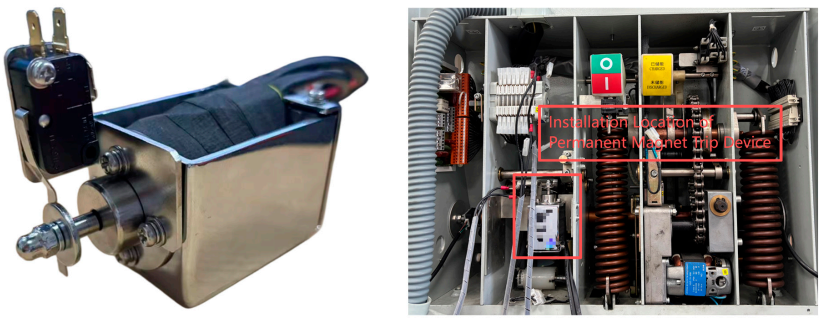


(**a**) (**b**)

**Figure 14.** Prototype of permanent magnet trip device and installation diagram. (**a**) Prototype of Permanent Magnet Trip Device; (**b**) Permanent Magnet Trip Device Installation Location.

By adjusting the control voltage of the permanent magnet trip device coil via an adjustable DC power supply, an auxiliary switch is inserted into the control circuit. Once the contacts are fully separated, the auxiliary switch interrupts the control circuit, causing the coil current to decrease. The duration of this period correlates with the speed of the mechanism's operation—the faster the mechanism moves, the greater the rate of current decay. By collecting coil current through Hall current sensors and measuring the rotation angle of the trip arm via angular displacement sensors, the core travel of the permanent magnet trip device was determined. The adjusted experimental results are as follows:

- In the trip performance test of the permanent magnet trip device, the trip time and trip coil current of the permanent magnet trip device during the tripping process were measured at a rated voltage of DC 220 V. The relationship between the trip coil current and the equivalent travel of the moving iron core is shown in Figure 15. The trip time was 14.56 ms (simulation value: 14.10 ms), the trip coil current was 1.456 A (simulation value: 1.432 A), with the error in the simulation results kept within 5%.
- When the DC voltage reaches 74 V (32% of rated voltage) or below, the permanent magnet trip device does not operate, and the circuit breaker operating mechanism does not release or trip. When the DC voltage reaches 130 V (59% *Un*) or above, the permanent magnet trip device operates. When the DC voltage reaches 135 V (61% *Un*) or above, the permanent magnet trip device achieves automatic reset, meeting technical requirements.
- Multiple measurements of the permanent magnet trip device's operating time yielded the results shown in Table 11. As indicated in Table 8, the average operating time of the permanent magnet trip device is 14.49 ms, with a standard deviation of 1.04 ms, demonstrating low data dispersion. During actual operation, the permanent magnet trip device enables the circuit breaker to trip within 20 ms, achieving the objective of rapid fault clearance.

**Table 11.** Test results for operating times of permanent magnet trip devices.

| | Rated Control Voltage DC 220 V | | |
|---|---|---|---|
| **Group** | **Traditional Solenoid-Type Electromagnetic Trip Device** | **Permanent Magnet Trip Device** | **Reduction Ratio** |
| 1 | 25.6 ms | 14.56 ms | 43.13% |
| 2 | 26.3 ms | 14.98 ms | 43.04% |
| 3 | 27.1 ms | 14.35 ms | 47.05% |
| 4 | 27.5 ms | 13.94 ms | 49.31% |
| 5 | 24.9 ms | 14.68 ms | 41.04% |
| 6 | 26.6 ms | 14.13 ms | 46.88% |
| 7 | 28.1 ms | 14.92 ms | 46.90% |
| 8 | 26.9 ms | 13.96 ms | 48.10% |
| 9 | 25.8 sm | 14.77 ms | 42.75% |
| 10 | 27.3 ms | 14.58 ms | 46.59% |

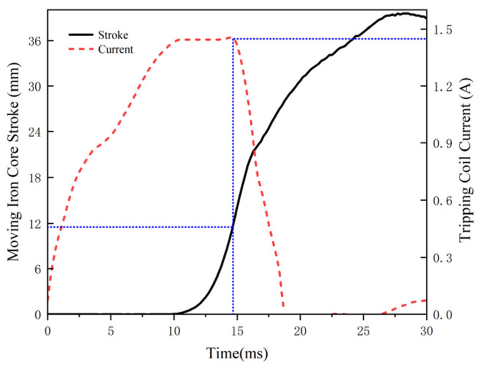


**Figure 15.** Test of permanent magnet trip coil current and moving core travel of moving contact.

## 6. Conclusions

This paper employs a research methodology that combines theoretical analysis, orthogonal experimental design, the BP-NSGA-II algorithm, Maxwell simulation, and experimental validation to optimize the design of a permanent magnet trip device and draws the following conclusions:

- Compared to the initial design, the optimized solution from the orthogonal test method reduced the trip time from 16.0 ms to 14.1 ms, achieving an 11.8% performance improvement that meets design requirements. The permanent magnet dimensions were optimized from $8 \times 44 \times 5$ mm to $6.5 \times 44 \times 5$ mm, increasing material utilization by 18.7%. The trip coil was optimized from a 0.18 mm wire diameter (2000 turns) to a 0.14 mm wire diameter (1400 turns), reducing coil material usage by 22.3% and coil volume by 30.0%. The mass of the moving assembly was reduced from 128.9 g to 114.1 g, representing an 11.5% decrease. The optimization scheme achieved substantial improvements in tripping time and material utilization, resulting in an overall enhancement of comprehensive performance.
- The simulation results from the digital prototype (14.1 ms) showed an error within 5% of the measured results from the physical prototype (14.56 ms). This demonstrates that electromagnetic finite element simulation software can be used to analyze the dynamic characteristics of permanent magnet trip devices, thereby improving design efficiency.
- The error between the results obtained using the BP-NSGA-II algorithm (13.86 ms) and those from finite element simulation (14.1 ms) is within 5%, indicating that the BP-NSGA-II algorithm can effectively replace time-consuming finite element simulation to improve optimization efficiency.
- Permanent magnet trip devices can replace traditional solenoid-type electromagnetic trip devices in circuit breakers, reducing the circuit breaker's tripping time from the original 25–40 ms to within 20 ms.
- The optimization design method for a permanent magnet trip device based on orthogonal experiments provides an effective approach to solving performance optimization problems in multi-parameter coupled systems, demonstrating significant engineering application value for enhancing the overall performance of permanent magnet trip devices.

**Author Contributions:** Conceptualization, J.Z. and Y.Y.; methodology, D.D. and K.Z.; software, K.Z. and L.Z.; validation, K.Z. and L.Z.; formal analysis, L.Z. and J.X.; data curation, J.L. and D.D.; writing—original draft preparation, Y.W. and J.X.; writing—review and editing, Y.W. and J.L.; funding acquisition, J.Z. and Y.Y. All authors have read and agreed to the published version of the manuscript.

**Funding:** This research was funded by the China Southern Power Grid Science and Technology Project, grant number 030100KC23100011(GDKJXM20231074).

**Data Availability Statement:** Data available on request due to restrictions, e.g., privacy or ethical. The data presented in this study are available on request from the corresponding author. These data are not disclosed to the public due to the commercial secrecy of the enterprise's production activities.

**Conflicts of Interest:** The authors declare no conflicts of interest. Authors Jie Zhang and any other CSG author are employed by China Southern Power Grid. The remaining authors declare that the research was conducted in the absence of any commercial or financial relationships that could be construed as a potential conflict of interest. No other competing interests exist.

## References

1. Zhong, J.; Chen, G.; Tan, S.; Yao, Y.; Wei, J. Key technologies and development trends of high-voltage switchgear. *High Volt. Eng.* **2021**, *47*, 2769–2782.

2. Hui, Y.F.; Duan, X.H.; Guo, L.C.; Ge, G.L.; Huang, J.Y.; Chen, Z.C. Research on the influence of opening latch system of spring mechanism on opening time of high voltage circuit breaker. *High Volt. Appar.* **2024**, *60*, 37–42.
3. Liu, C.; Zhang, Q.; Su, J.F.; Zhang, J.; Ding, S.S. Calculation and analysis of solenoid electromagnet for spring operating mechanism. *High Volt. Appar.* **2020**, *56*, 91–96.
4. Liu, Y.; Guan, C.; Yao, X.F.; Geng, Y.S.; Wang, J.H. Technical research and development of 72.5kV fast vacuum circuit breaker. *High Volt. Appar.* **2024**, *60*, 11–19.
5. Yan, F.; Ruan, J.; Liu, Y.; Chen, Z.; Zhuang, X.; Tang, C. Model-Aided State Parameter Inversion Identification of Electromagnetic Trip Device for High Voltage Circuit Breakers. *High Volt.* **2025**, *11*, 284–296. [CrossRef]
6. Wang, Z.; Sun, L.; He, S.; Geng, Y.; Liu, Z. A Permanent Magnetic Actuator for 126 kV Vacuum Circuit Breakers. *IEEE Trans. Magn.* **2014**, *50*, 129–135. [CrossRef]
7. Zhao, T.; You, Y.M.; Sang, Z.Q.; Wang, Y.Q.; Liu, J.W. Analysis of operating characteristics of permanent magnet solenoid for spring mechanism. *High Volt. Appar.* **2025**, *61*, 72–79.
8. Ye, X.R.; Chen, H.; Liang, H.M.; Chen, X.J.; You, J.X. Multi-Objective Optimization Design for Electromagnetic Devices With Permanent Magnet Based on Approximation Model and Distributed Cooperative Particle Swarm Optimization Algorithm. *IEEE Transactions on Magnetics* **2017**, *54*, 1–5.
9. Ma, Y.; Wang, D.; Shen, Y. Modeling and Multi-Objective Optimization Design of High-Speed on/off Valve System. *Appl. Sci.* **2024**, *14*, 7879. [CrossRef]
10. Yu, Y.; Zhao, P.; Hao, Y.; Zeng, D.; Hu, Y.; Zhang, B.; Yang, H. Multi Objective Optimization of Permanent Magnet Synchronous Motor Based on Taguchi Method and PSO Algorithm. *Energies* **2023**, *16*, 267. [CrossRef]
11. Zhong, Q.; Wang, J.; Xu, E.; Yu, C.; Li, Y. Multi-objective optimization of a high speed on/off valve for dynamic performance improvement and volume minimization. *Chin. J. Aeronaut.* **2024**, *37*, 435–444. [CrossRef]
12. Tang, Z.H.; Xu, Z.H. Optimal Design Method for AC Contactor Spring System Based on Response Surface Method. *Trans. China Electrotech. Soc.* **2022**, *37*, 515–527.
13. Jiang, J.; Lin, H.; Fang, S. Optimization Design of a Permanent Magnet Actuator for 126-kV Vacuum Circuit Breaker. *IEEE Trans. Appl. Supercond.* **2018**, *28*, 06001. [CrossRef]
14. Zhang, S.; Yan, H.; Yang, L.; Gao, J.; Chen, J. Optimization Design of Permanent Magnet Synchronous Motor Based on Multi-Objective Artificial Hummingbird Algorithm. *Actuators* **2024**, *13*, 243. [CrossRef]
15. Gao, F.; Ren, L.; Zhang, B.J.; Han, G.; Li, G.F. Optimal design of energy storage capacitor for 40.5 kV vacuum circuit breaker electromagnetic repulsion mechanism based on orthogonal experimental design. *High Volt. Appar.* **2017**, *53*, 223–229.
16. Sun, J.; Cai, J.G.; Ge, X.F.; Guo, Q.; Zheng, Y. Performance optimization of two-blade bulb tubular turbine based on orthogonal test with multiple objectives. *Proc. CSEE* **2022**, *42*, 3317–3327.
17. Ding, C.; Ding, Y.; Yuan, Z.; Li, J. Structural optimization design of electromagnetic repulsion mechanism based on BP neural network and NSGA-II. *IEEJ Trans. Electr. Electron. Eng.* **2023**, *18*, 1914–1922. [CrossRef]
18. Jiang, J.J.; Lin, H.; Fang, S. Multi-objective optimization of a permanent magnet actuator for high voltage vacuum circuit breaker based on adaptive surrogate modeling technique. *Energies* **2019**, *12*, 4695. [CrossRef]
19. Huang, S.; Yan, B.; Xia, B. Multi-objective Optimization of Electromagnetic Devices Based on Improved Jaya Algorithm and Kriging Model. In *The Proceedings of the 16th Annual Conference of China Electrotechnical Society: Volume I*; Springer: Singapore, 2022; pp. 125–132.
20. Liu, T.; Li, R.Y.; Zhou, L.; Shi, X.N.; Wei, Z.Y.; Ren, M.; Gou, X.Y. Research progress on coercivity enhancement technology of sintered Nd-Fe-B magnets. *J. Chin. Soc. Rare Earths* **2024**, *43*, 1–19.
21. He, J.J.; Yuan, Z.; Jing, X.; He, J.; He, B. Review on electromagnetic repulsion mechanisms. *High Volt. Eng.* **2017**, *43*, 3809–3818.
22. *GB/T 11022-2020*; SAC/TC 65. Common Specifications for High-Voltage Alternating-Current Switchgear and Controlgear Standards. China Standard Press: Beijing, China, 2020.
23. *GB/T 6983-2022*; Electromagnetic Pure Iron. Standards Press of China: Beijing, China, 2022.
24. Su, X.P.; Tian, H.B.; Mu, S.Y. Structural design and optimization of electromagnetic system for intelligent AC contactor. *Electr. Mach. Control* **2020**, *24*, 43–50.
25. Cao, W.B.; Fang, R.Q.; Yang, G.L.; Zhao, T.; Yu, Z. Optimisation Analysis and Validation of Force-stroke Characteristics of Explosion-proof Electromagnets. *Chin. Hydraul. Pneumat.* **2024**, *48*, 12–21.
26. Zhu, M.M.; Pan, W.J.; Liu, X. Interactive genetic algorithm based on BP nerual network and user cognitive surrogate model. *Comput. Eng. Appl.* **2020**, *56*, 146–151.

27. Xu, Y.J.; Xu, F.F. Optimization of Activation Function in Neural Network Based on ArcReLU Function. *J. Data Acquis. Process.* **2019**, *34*, 517–529.
28. Feng, S.G.; Ai, Q. Application of Fast and Elitist Non-Dominated Sorting Generic Algorithm in Multi-Objective Reactive Power Optimization. *Trans. Electrotech. Soc.* **2007**, *22*, 146–151.